Transition metal-based high entropy alloy microfiber electrodes: Corrosion behavior and hydrogen activity

Baran Sarac [a, *], Vladislav Zadorozhnyy [b], Yurii P. Ivanov [c, d], Florian Spieckermann [i], Semen Klyamkin [e], Elena Berdonosova [e], Mikhail Serov [f], Sergey Kaloshkin [b], A. Lindsay Greer [c], A. Sezai Sarac [g, h], Jürgen Eckert [a, i, j]

[a] Erich Schmid Institute of Materials Science, Austrian Academy of Sciences, Jahnstraße 12, 8700 Leoben, Austria
[b] National University of Science and Technology "MISIS", Leninsky prosp., 4, 119049 Moscow, Russia
[c] Department of Materials Science & Metallurgy, University of Cambridge, Cambridge CB3 0FS, UK
[d] School of Natural Sciences, Far Eastern Federal University, 690950 Vladivostok, Russia
[e] Department of Chemistry, M.V. Lomonosov Moscow State University, 119991 Moscow, Russia
[f] Moscow Aviation Institute (National Research University), 125993 Moscow, Russia
[g] Department of Chemistry, Istanbul Technical University, 34469 Istanbul, Turkey
[h] Polymer Science & Technology, Istanbul Technical University, 34469 Istanbul, Turkey
[i] Department of Materials Science, Chair of Materials Physics, Montanuniversität Leoben, Jahnstraße 12, 8700 Leoben, Austria
[j] Adjunct with National University of Science and Technology "MISiS", Leninsky Prosp., 4, 119049 Moscow, Russia

ARTICLE INFO

Keywords:
High entropy alloy
EIS
STEM
Alkaline corrosion
Passive film
gas-solid reactions

ABSTRACT

This contribution reveals ultra-high corrosion resistance of high entropy alloys (HEAs), i.e. $Ti_{20}Zr_{20}Nb_{15}V_{15}Hf_{15}Ta_{15}$ of 1.85 μm yr^{-1} in alkaline environment, adverting their use for battery/fuel cell components. Formation of several nanometers passive oxide layer confirmed by scanning transmission electron microscopy accounts for corrosion resistance which increases with TiO_x content. Cathodic Tafel slope of 67 mV dec^{-1} and large transfer coefficient of 0.82 obtained for $Ti_{20}Zr_{20}Nb_{20}V_{20}Ta_{20}$ suggest its use for hydrogen electrocatalysis. High amounts of hydrogen storage, 1.7 wt% in $Ti_{25}Zr_{25}Nb_{15}V_{15}Ta_{20}$, were confirmed by gas-solid reactions. This HEA also has high corrosion resistance in acidic and saline environments ideal for coatings and surgical tools/implants.

1. Introduction

The hydrogen evolution reactions using advanced alloy systems have a growing interest in recent years owing to the poor kinetics, i.e., sluggish water dissociation step, of the conventionally used materials in alkaline electrolytes. The main difference between acidic and alkaline media is the low number of protons in an alkaline environment. Hence, a water-dissociation step is expected to detach the bonded hydrides and form H_2 molecules [1,2]. This slow kinetics challenge the further advancement of the anionic exchange membrane water electrolyzer.

High entropy alloys are a new class of materials containing five or more principal elements in an equimolar or near-equimolar composition. The presence of different elements increases the configurational entropy of mixing, which can surpass the enthalpies of compound formation, and in turn, do not permit the formation of undesired intermetallics phases nor the segregation [3]. In this way, a higher number of principal elements yields the formation of random solid solutions during solidification. The lowering of free energies by the high entropy of mixing results in simple solid-solution phases out of main constituents, which does not allow complex phases, including oxides, carbides or silicides within the bulk but only on the surface [4,5]. So far, studies of various high and medium entropy alloys, HEA and MEA, respectively, have been tested in aqueous environments to understand the electrocatalytic and electrocorrosion behavior along with diffusion and electron transfer kinetics [6–15]. Due to the differences in electronic structures and valence states, transition group elements display remarkable differences in terms of hydrogen evolution reaction (HER). For example, group IVB (Ti, Zr, Hf) and VB (V, Nb, Ta) elements have strong M—H bond strengths and are excellent hydride formers [16,17]. Besides, the large difference in elemental atomic radii (cf. 208 pm and 171 pm for Hf and V, respectively) is expected to induce an enhanced electrocatalytic behavior in analogy to the large lattice distortions upon

* Corresponding author.
E-mail address: baran.sarac@oeaw.ac.at (B. Sarac).

hydrogen absorption during gas-solid reactions of a similar TiVZrNbHf HEA alloy.[16] Moreover, for the bio-implant applications, similar multicomponent alloy systems have been recently tested in different buffer solutions and saline environments [18–22].

This study focuses on the (bio)corrosion kinetics and electrocatalytic activity of newly developed high entropy alloy, $Ti_{20}Zr_{20}Nb_{20}V_{20}Ta_{20}$ (HEA1), and $Ti_{25}Zr_{25}Nb_{15}V_{15}Ta_{20}$ (HEA2) and $Ti_{20}Zr_{20}Nb_{15}V_{15}Ta_{15}Hf_{15}$ (HEA3) compositions derived from HEA1. Linear sweep voltammetry (LSV) in 1 M KOH solution is utilized to assess the corrosion potential and current stability. Moreover, the charge transfer coefficients calculated from the linear anodic, β_a, and cathodic, β_c, parts are used to compare the annual corrosion rates in the same electrolyte. A newly introduced approach by our group via the fitting of the non-linear anodic and cathodic parts to the Butler–Volmer (B–V) model is applied to these entropy alloys [23], which enabled the transfer coefficient, α, and the exchange current density j_0 of such alloys to be calculated and evaluated for the first time. Electrochemical impedance spectroscopy (EIS) data measured at instantaneous open circuit potential is fitted by an equivalent circuit model, which provides solution and charge transfer resistance, and constant phase element parameters related to double-layer capacitance. Local structural analysis by synchrotron X-ray diffraction (XRD) confirms the single-phase BCC structure. A cross-sectional investigation of the as-sputtered and used electrodes performed by the high-resolution (scanning) transmission electron microscopy marks the influence of oxide formation upon potentiodynamic polarization.

2. Experimental

2.1. Materials preparation

The chips of Zr (purity 99.5%), Ti (purity 99.5%), V (purity 99.7%), Nb (purity 99.95%) Hf (purity 99.5%) and Ta (purity 99.95%) were used for the preparation of the billets by arc-melting. Electron beam melting with pendant drop melt extraction (EBM-PDME) produce continuous and discrete fibers where the powder sizes are smaller than by traditional spraying techniques [24,25]. Rapidly quenched fibers were developed by the electron beam melting of the billet material in a vacuum facility. In the EBM-PDME method, the lower end of a vertically arranged billet melts with the formation of a hanging melt drop. The molten drop touches the tip of the rotating cooled heat absorber in the shape of an isosceles triangle, and subsequently solidifies in the zone of the contact. The fiber-formed material is detached from the tip of the working edge because of centrifugal forces. The method of extraction of melt to obtain fine particles was used to retain high cooling rates of the melt (up to 10^6 K s^{-1}), yielding a microcrystalline or amorphous structure. The adopted production method enables for production of refractory and chemically active materials with the crucible-free melting mode [26–28]. The developed compositions are $Ti_{20}Zr_{20}Nb_{20}V_{20}Ta_{20}$ (HEA1), $Ti_{25}Zr_{25}Nb_{15}V_{15}Ta_{20}$ (HEA2) and $Ti_{20}Zr_{20}Nb_{15}V_{15}Ta_{15}Hf_{15}$ (HEA3). For all the post-characterization steps, since samples are very thin and round, in order not to damage the samples, no polishing was applied on the surface.

2.2. Synchrotron X-ray diffraction

Samples were tested as is (after cleaning in ethanol and rinsing) at P02.1 the High Resolution Powder Diffraction Beamline at PETRA III. The X-ray beam dimensions were tuned to 200 × 200 μm^2 and recorded with a 2048 × 2048 pixels Perkin Elmer XRD1621 CN3 – EHS detector. The sample distance to the detector was 1.612 m. The X-ray source has high flux (~ 10^{10} photons/s monochromatic beam) and high energy (60 kV).

2.3. Scanning electron microscopy and energy dispersive X-ray and optical microscopy

The produced microfibers were cleaned in a sonication bath using acetone, isopropanol, and ethanol in respective order for 5 min in each organic solution. The samples were subsequently rinsed by distilled water followed by air blow fast-drying. The fiber was fixed on the standard aluminum stub by conducting carbon pad. The microstructure of the microfibers was examined by scanning electron microscopy (SEM) "Zeiss Ultra 55" carried out at 15 kV, equipped with an energy dispersive X-ray spectrometer (EDS) "Bruker".

The optical micrographs used in the surface area measurement were recorded by Olympus BX51 Fluorescence Microscope using the Olympus Stream Motion 1.9.3. software – Extended Focal Imaging feature. By capturing the entire depth, the actual surface area was determined using Gwyddion SPM data visualization and analysis software from the analysis of 20 × 20 μm^2 regions registered from the middle of each sample. The submerged surface areas for each microfiber were measured to be 0.0463 ± 0.003 cm^2 (HEA1), 0.0214 ± 0.003 cm^2 (HEA2), and 0.0232 ± 0.003 cm^2 (HEA3).

2.4. HAADF STEM/EDX

AT represen[illegible]sen, and after rinsing the samples with is[illegible] to get rid of any residues from sample preparation, the protective rectangular Pt layer with dimensions (15 μm length, 2 μm width and 2 μm thickness) were deposited by an electron beam prior to FIB cutting. A cross-sectional specimen with final thicknesses of 100 nm was prepared by FIB milling using a Helios Nanolab FIB/SEM (Thermo Fisher Scientific). The prepared specimen was transferred from the sample to a standard grid for TEM. Final polishing was done at a reduced voltage of 2 kV, which minimizes the size of the damaged material and reduces implanted gallium levels in the thin foil. Transmission electron microscopy (TEM) imaging of the samples was performed using an FEI Tecnai Osiris microscope with field emission gun operated at 200 kV equipped with Super-X windowless EDX detector for high-resolution elemental mapping. The Energy dispersive X-ray (EDX) experiments were conducted in scanning TEM mode with a high-angle annular dark-field (HAADF) detector and a ~ 0.2 nm probe diameter. SAED patterns and associated images were retrieved with a Gatan US1000 charge-coupled device camera.

2.5. Hydrogen storage

Hydrogen storage performance of the HEAs was studied on cast alloys. Prior to measurements, the samples weighing 2 g with a precleaned surface were crushed to a coarse powder and then placed in a steel reactor. The reactor was connected to a Sieverts-type measuring system equipped with a vacuum pump and a source of pure (99.999%) hydrogen. [29]. The HEAs were subjected to activation in vacuum (0.67 Pa) for 2 h at a temperature of 220–400 °C depending on the alloy composition. Hydrogenation was performed at the same temperature under a hydrogen pressure of 6 MPa. The amount of hydrogen absorbed was determined from pressure changes in the measuring system with calibrated volume. The composition of the formed hydride was calculated using the van der Waals equation for highly compressed non-perfect hydrogen.

2.6. Electrochemical study

All the electrochemical measurements were performed using a PARSTAT 4000A Potentiostat Galvanostat (Princeton Applied Research, USA), with 30 μV applied voltage resolution for ± 1 V signal and 1 μs time-base resolution. Data was acquired via VersaStudio 2.60.6 software. The potentials in this study are provided with respect to Ag/AgCl

with saturated KCl solution with a redox potential of +0.197 V vs. a standard hydrogen electrode at 25 °C. The term overpotential, the shift of the actual potential E from the equilibrium state E° ($\eta = E - E^{\circ}$), is used to define the cathodic and anodic reactions [30]. 5 mL 1 M KOH solution was prepared with deionized water and flushed with argon gas for 15 min to minimize the impurities. A new solution is used for each composition. A different single as-spun microfiber with a length of ~ 2 cm was used for each experiment. All the microfibers were cleaned and dried following the steps in SEM sample preparation. Linear potential sweep voltammograms (LSV) were registered at a sweep rate of 5 mV s^{-1} from −1.3 to 0 V with a shift in onset potential of 0.1 V until 1 V. The polarization was started from a highly cathodic side to obtain a cleaner and corrosion-free surface of the specimen and thus to determine the hydrogen evolution and anodic reactions more accurately over a longer range. Moreover, potentiodynamic polarization was performed after argon-deaeration via a potentiostatic hold to minimize as much as possible the air-formed oxide, which adjusts the reduction potential of the Nernst potential upon polarization. Tafel fit function of the VersaStudio was utilized to measure the cathodic β_c and anodic β_a Tafel fits, corrosion current density j_{corr} and potential E_{corr}. The electrochemical impedance spectroscopy (EIS) measurements at open circuit potential (OCP) at an ac amplitude of 10 mV were recorded from 100,000 Hz to 0.1 Hz. The simulation of the EIS data was conducted with the electrical equivalent circuit of R(QR) using the ZSimpWin V.3.10 analysis program.

2.7. Physical parameters

The equivalent weight EW of each alloy was calculated from $EW = 1/\sum \frac{f_i n_i}{a_i}$, where f_i, n_i and a_i are mass fraction, electrons exchanged, and atomic weight, respectively, of the i^{th} alloying element. The theoretical alloy density T is determined from the equation $\frac{1}{T} = \sum_{i=1}^{n} \frac{\omega_i}{T_i}$. Here, T_i is the density of each component and ω_i is the mass fraction of each component within the alloy, where $\sum_{i=1}^{n} \omega_i = 1$.

3. Results and discussion

3.1. Morphological investigation of microfibers

The morphology of the ion-plasma sputtered microfibers is shown in Fig. 1a, b. The rods have an average diameter of 65–70 μm with a rough cross-sectional surface. The oxide particles of several microns are observed on the microfiber surface (Fig. 1c). A digital image of the bundle of microfibers is shown in Fig. 1d.

3.2. XRD investigation of microfibers

The synchrotron X-ray diffraction patterns (Fig. 2) confirm the single HEA phase for each composition taken at 200 μm × 200 μm beam dimension with [Edit] [Proof] [PDF] 20662 Å. Lattice parameters of the BCC phase extracted from the peak positions are a_{HEA1}

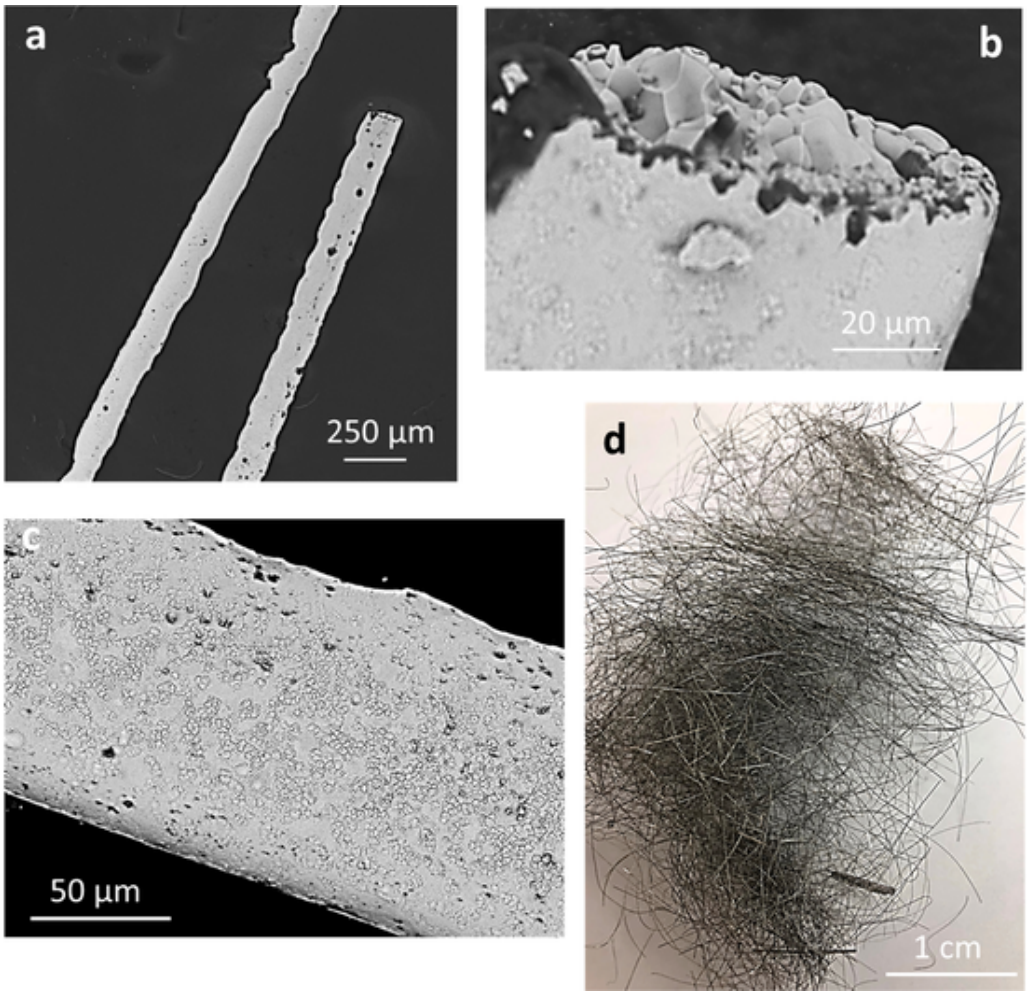

Fig. 1. (a) SEM micrograph of microfibers of a representative HEA2 sample, and (b) their cross-section. (c) The second phase is observed on the microfiber surface for all the compositions (the image is taken from the HEA3 sample). (d) Digital photo of the bundle of the HEA1 microfibers.

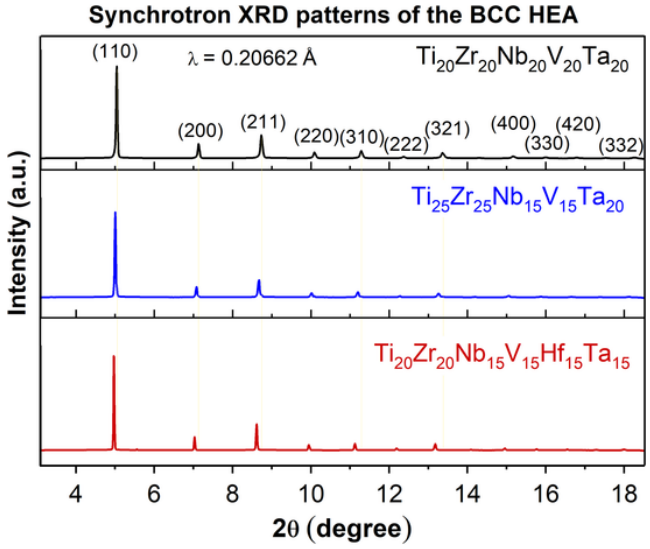

Fig. 2. Synchrotron XRD diffractograms of the HEA1, HEA2 and HEA3 samples. The indexed peaks show the miller indices of the BCC unit lattice for all the investigated compositions. Yellow lines indicate shifts in the reflections as a function of composition.

$= 3.323 \pm 0.001$ Å, $a_{HEA2} = 3.347 \pm 0.002$ Å, and $a_{HEA3} = 3.370 \pm 0.003$ Å.

3.3. Interaction with gaseous hydrogen

The hydrogen storage capacities of the obtained samples are presented in Table 1. It is important to note that hydrides with very high thermal stability formed even at low equilibrium desorption pressure and elevated temperatures. This condition did not allow us to measure pressure-composition isotherms under experimental conditions.

3.4. Corrosion polarization behavior

The electrocatalytic activity of the high entropy alloys was examined in 1 M KOH solution using a standard three-electrode system at a scan rate of 5 mV s^{-1} via linear sweep voltammetry.

High stability, particularly for the $Ti_{25}Zr_{25}Nb_{15}V_{15}Ta_{20}$ (HEA2), is observed, where the sweep lines coincide with each other. The corresponding potentiodynamic polarization curve (E vs. log j) shows only a very slight shift of the corrosion potential, $\Delta E_{corr} = 5$ mV (from −451 mV to −446 mV), as the onset potential of the LSV shifts from −1.3 V to −1 V (Fig. 3a). This difference for $Ti_{20}Zr_{20}Nb_{15}V_{15}Hf_{15}Ta_{15}$ (HEA3) is $\Delta E_{corr} = 27$ mV (from −541 mV to −514 mV), and for the $Ti_{20}Zr_{20}Nb_{20}V_{20}Ta_{20}$ (HEA1) (from −618 mV to −674 mV) $\Delta E_{corr} = 56$ mV. Fig. 3b shows that the highest E_{corr} is observed for the HEA2, where the lowest corrosion current of $j_{corr} = 6.58$ nA cm^{-2}, is observed for the Hf containing HEA3. The potentiodynamic polarization curves recorded between −1.5 and 0 V show the shift of the corrosion potential of the HEA1 ($E_{corr} = -575$ mV) towards positive direction, i.e. $E_{corr} = -497$ mV for HEA3 and $E_{corr} = -456$ mV for HEA2. Moreover, the corrosion current density of the HEA1 ($j_{corr} = 435$ nA cm^{-2}, where the measurement is shown in Fig. 3c) decreases to 234 nA cm^{-2} (HEA2) and to 170 nA cm^{-2} (HEA3). These findings indicate better corrosion resistance in the alkaline environment for the newly developed HEA2 and HEA3 alloys. All the considered HEAs have a lower j_{corr} compared to that of the 304 SS in 1.5 M NaOH solution ($j_{corr\_304\ SS} = 460$ nA cm^{-2}) [31]. Table 2 shows the parameters retrieved from the Tafel fit measurements and intrinsic properties. The average corrosion rate, V_{acr} (micrometer per year, μm yr^{-1}), is calculated from [32]:

$$V_{acr} = \frac{3.27 \times j_{corr} \times EW}{T}, \quad (1)$$

where j_{corr} has units of μA cm^{-2}, EW is the equivalent weight, and T is the theoretical density of alloy. Hence HEA3 (1.85 μm yr^{-1}) < HEA2 (2.64 μm yr^{-1}) < HEA1 (4.87 μm yr^{-1}). Furthermore, no pitting corrosion is observed for the HEA2 and HEA3, confirming that they are better than the HEA1 in the alkaline medium.

The hydrogen sorption and evolution kinetics were defined by Butler–Volmer non-linear fitting, which was applied on the LSV curve. This is an approximate form of the current-overpotential equation, which neglects the mass transfer effects while the currents are kept very low [33]. The transfer coefficient α defines the activation free energy barrier. In alkaline conditions the chance of insertion of a free proton in solution is almost [Edit] [Proof] [PDF] lmer step (proton adsorption and dischar ut by a water dissociation reaction which is presumably accompanied by the Volmer reaction and happens separately before the Volmer reaction in the vicinity of the electrode [34]. The electrochemical hydrogen desorption is described by the Heyrovsky reaction (Eq. (3)). In this reaction, the instantly absorbed hydrogen intermediate HEA-H joins preferably with a proton and electron concurrently and yields H_2 molecules [35]. Since the reaction occurs in an alkaline environment, both Volmer and Heyrovský steps depend on water dissociation to form $H_{ads}/H_{2(g)}$. Instead of a dissociative step, H_{ads} can directly join and form H_2 depending on the reaction kinetics as the Tafel slope approaches 30 mV dec^{-1} (Tafel reaction). The cathodic Tafel slope in our study is measured as 82 mV dec^{-1}. It is known that any HER electrocatalyst that has a Tafel slope value lesser than 120 mV dec^{-1}but higher than 60 mV dec^{-1} is considered to have good electrocatalytic activity in alkaline solution, and the interface follows the Volmer–Heyrovský mechanism [36]. Hence the two-step HER mechanism in an alkaline medium is [34]:

$$HEA + H_2O + e^- \rightleftharpoons HEA\text{–}H_{ads} + OH^-_{(aq)}, \quad (2)$$

$$HEA\text{–}H_{ads} + H_2O + e^- \rightleftharpoons HEA + OH^-_{(aq)} + H_{2(g)}. \quad (3)$$

From the Volmer and Heyrovský steps of alkaline HER, it can be deduced that the interface is an extra burden to carry the water dissociation step providing the required free proton for the reaction to proceed. This evidences that HER in alkali is harder than acidic HER. The overall reaction with hydroxide ions in alkaline media is written as (Eq. (4)) [37]:

$$2H_2O + 2e^- \rightleftharpoons H_2 + 2OH^-_{(aq)}. \quad (4)$$

Hence, the resultant cathodic and anodic reaction can be described in B–V fitting by the assumed Volmer–Heyrovský steps (Eq. (5)) as [38]:

$$j = j_0 \cdot \left\{ \frac{x_{H_2}}{x_{H_2,ref}} \exp\left(-\frac{\alpha n F \eta}{RT}\right) - \frac{x_{H_2O}}{x_{H_2O,ref}} \exp\left(\frac{(1-\alpha) n F \eta}{RT}\right) \right\}, \quad (5)$$

here j is the current density, j_0 the exchange current under equilibrium conditions, F the Faraday constant (96,485 A s mol^{-1}), n the number of electrons involved in the electrode reaction, R the gas constant (8.314 J K^{-1} mol^{-1}) and T the temperature at which the measurements

Table 1
Comparison of the selected alloys in terms of hydrogen storage capacity in mass percent.

Alloy composition	Hydrogen storage capacity, mass% (error within ± 0.1%)
$Ti_{20}Zr_{20}V_{20}Nb_{20}Ta_{20}$ (HEA1)	1.6
$Ti_{25}Zr_{25}V_{15}Nb_{15}Ta_{20}$ (HEA2)	1.7
$Ti_{20}Zr_{20}V_{15}Nb_{15}Ta_{15}Hf_{15}$ (HEA3)	1.5

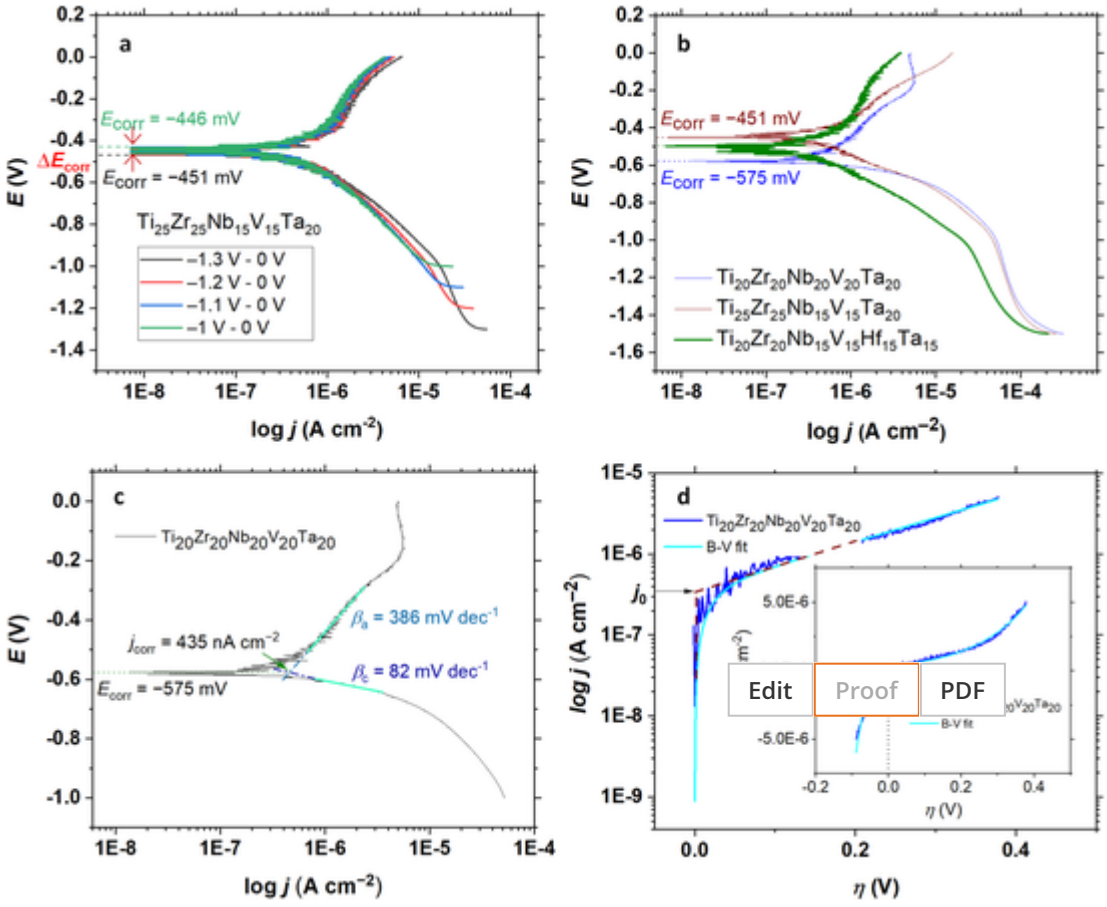

Fig. 3. (a) Potentiodynamic polarization of the representative $Ti_{25}Zr_{25}Nb_{15}V_{15}Ta_{20}$ (HEA2), confirming very high stability in terms of E_{corr} and j_{corr}. A shift in onset potentials from −1.3 V to −1 V was applied, where the scanning at each curve was until 0 V. (b) Comparison of the potentiodynamic polarization curves of HEAs between −1.5 V and 0 V. (c) Determination of E_{corr} and j_{corr} for the representative $Ti_{20}Zr_{20}Nb_{20}V_{20}Ta_{20}$ (HEA1) from the intersection of linear slopes of the anodic β_a and cathodic β_c parts. The anodic and cathodic Tafel slopes are determined from the linear regions indicated by light green. All potentials are with respect to Ag/AgCl (3 M NaCl), where its redox potential is +0.197 V vs. a standard hydrogen electrode at 25 °C. (d) log j vs. overpotential η curve (blue) and the Butler–Volmer (B–V) fitting (cyan) of the representative HEA1 sample. j_0 is measured from the y-intercept (η = 0) of the log j vs. η graph. The corresponding j_0 values are –3.6 × 10^{-4} for HEA1, –4.5 × 10^{-5} for HEA2 and –5.3 × 10^{-6} for HEA3. The intersection of vertical and inclined parts of the B-V curves j vs. η showing the measured curve profile and the fitting are given in the inset. All measurements are conducted at a sweep rate of 5 mV s^{-1}. (For interpretation of the references to color in this figure legend, the reader is referred to the web version of this article.)

Table 2
Comparison of different HEAs. T: theoretical alloy density, EW: the equivalent weight of the alloys, E_{corr}: corrosion potential, j_{corr}: exchange current density, V_{acr}: average corrosion rate, E_{pit}: pitting potential, β_a: anodic beta constant, β_c: cathodic beta constant.

Composition	T (g cm^{-3})	EW (-)	E_{corr} (mV)	j_{corr} (A cm^{-2})	V_{acr} (μm year^{-1})	E_{pit} until 0 mV	β_a (mV dec^{-1})	β_c (mV dec^{-1})
$Ti_{20}Zr_{20}Nb_{20}V_{20}Ta_{20}$ (HEA1)	8.469	28.78	−575	4.35 × 10^{-7}	4.87	−160 mV	386	82
$Ti_{25}Zr_{25}Nb_{15}V_{15}Ta_{20}$ (HEA2)	8.241	28.20	−456	2.34 × 10^{-7}	2.64	no	194	136
$Ti_{20}Zr_{20}Nb_{15}V_{15}Ta_{15}Hf_{15}$ (HEA3)	8.987	29.67	−498	1.70 × 10^{-7}	1.85	no	154	147

were performed (298 K). j_0 is determined from the y-intercept (η = 0) of the log j vs. η graph (Fig. 3d). In order to stay in (quasi)reversible potentials of the Tafel region close to equilibrium, a maximum current range of $\pm 5 \times 10^{-6}$ A cm^{-2} was selected (Fig. 3d inset), where this maximum current is below the limiting current reached at high η [39]. Since the mass transfer is negligible due to micro-electrode size, very small volume electrolyte solution (5 mL) and close positioning of anode and cathode electrodes, surface and bulk concentrations become identical and their ratio equals unity (as it was described in detail in [4]). Thus, Eq. (5) turns into a simplified B–V equation (Eq. (6)) [23,30,33]:

$$j = j_0 \cdot \left\{ \exp\left(-\frac{\alpha n F \eta}{RT}\right) - \exp\left(\frac{(1-\alpha) n F \eta}{RT}\right) \right\}. \quad (6)$$

The largest cathodic transfer coefficient of α = 0.82 with the highest $j_0 = -3.6 \times 10^{-4} + 3.3 \times 10^{-6}$ mA cm^{-2} is noted for the HEA1, referring to the highest hydrogen evolution reaction rate (Table 3). Similar α values were recorded for the forward (cathodic) reaction of the platinized nickel electrode in 0.1 M KOH solution at room temperature (α

Table 3
j0 and α calculated from the Butler–Volmer equation.

Composition	j_0 (mA cm^{-2})	α	R-squared
HEA1	–3.6 × 10^{-4} ± 3.3 × 10^{-6}	0.82	0.987
HEA2	–4.5 × 10^{-5} ± 8.1 × 10^{-7}	0.60	0.905
HEA3	–5.3 × 10^{-6} + 1.4 × 10^{-7}	0.64	0.745

= 0.75–0.8) [27]. For HEA1, larger hydrogen evolution is also confirmed by the smallest cathodic beta constant (β_c = 82 mV dec^{-1}) among the investigated compositions, calculated from the intersection of the linear parts of the anodic and cathodic parts of the V vs. log i curves. For this sample, the oxide layer mainly composed of Zr and Ti is the main reason for the high anodic beta constant (β_a = 386 mV dec^{-1}) as confirmed by the STEM-EDX analysis in Section 3.6. On the other hand, the HEA2 is closer to the symmetric electron transfer (α = 0.5), facilitating Faradaic oxidation/reduction. As expected, the calculated j_0 values are around three orders of magnitude lower than those for Pt and graphite electrodes [40]. Furthermore, these values are also lower than our previous study on Pd-thin film coatings on Si substrates [23]. Nevertheless, the amount of hydrogen evolution can be significantly increased using many microfibers, e.g. in a bundle or woven form.

3.5. Electrochemical impedance spectroscopy

The Nyquist plots of the HEAs show remarkable differences (Fig. 4a). The circuit $R(QR)$ provides a very good fit in terms of each parameter (error margins are provided in parenthesis) with a very small solution resistance R_1 values and overall chi-squared (Table 4). The difference in the solution resistance can correspond to the internal resistance of active electrodes with hydrogen, the contact resistance between the active material and electrode interface, and the electrolyte resistance [41]. For this reason, reference (RE) and counter (CE) electrodes and the contact clips of the RE, CE, and working electrode were polished, all the solutions before the experiments were re-prepared and flushed with Ar, and the measurements were repeated three times to avoid any external contribution originating from the contacts or electrolyte. In this way, the difference in the solution resistance R_s was determined to be stemming from the internal resistance of the individual nanofilms related to the composition differences. Furthermore, the resistance of the oxide altered by the increase in the Ti content in the oxide layer for the HEA3 sample (c.f. Ti/Zr = 0.36 for HEA1 and 0.77 for HEA3 for the natural oxide layer).

The smallest semi-circle is obtained for the HEA1 using the $R(QR)$ circuit model (inset), indicating its high electron activity due to low charge transfer resistance (see R_2 in Table 4). A very remarkable finding is that the phase angle reaches up to 85.0° (for HEA3) and retains above 80° for 3–4 orders of magnitude frequency difference (Fig. 4b). Similarly, the Bode magnitude plots for the electrodes show linearity except for the very high frequencies. This linearity over a wide range of frequencies indicates an excellent capacitance, possibly due to the growth of the oxide layer as confirmed by the HRTEM and HAADF-STEM analysis provided in Section 3.6 and Fig. S1 [42]. Moreover, very high R_2 values of 10^6–10^7 Ω confirm this highly semiconducting behavior on the outer microfiber layers.

Fig. 4c compares the R_2 and Q_0 parameters with β_c from the Tafel fitting and α from the B–V model. The increase in the EIS resistance R_2 is correlated to the accumulation of hydrogen nearby the working electrode [43] and hence yielding a larger cathodic Tafel coefficient β_c. The closest trend is observed between β_c and Q_0; an increase of the slope of the linear part of the log j vs. E curve leads to a proportional drop in the double-layer capacitance parameter. Besides, the transfer coefficient calculated from the combination of non-linear and linear parts has a linear relationship with Q for the HEA1 and HEA2 electrodes, where the deviation of the low confidence of the fit.

3.6. Structural investigation and hydrogen interactions

The cross-sectional imaging of the as ion-plasma sputtered samples by high-angle annular dark-field scanning transmission electron microscopy (HAADF-STEM) shown in Fig. S1a corroborates the smooth and flat interface between the protective Pt and HEA2. The enlarged

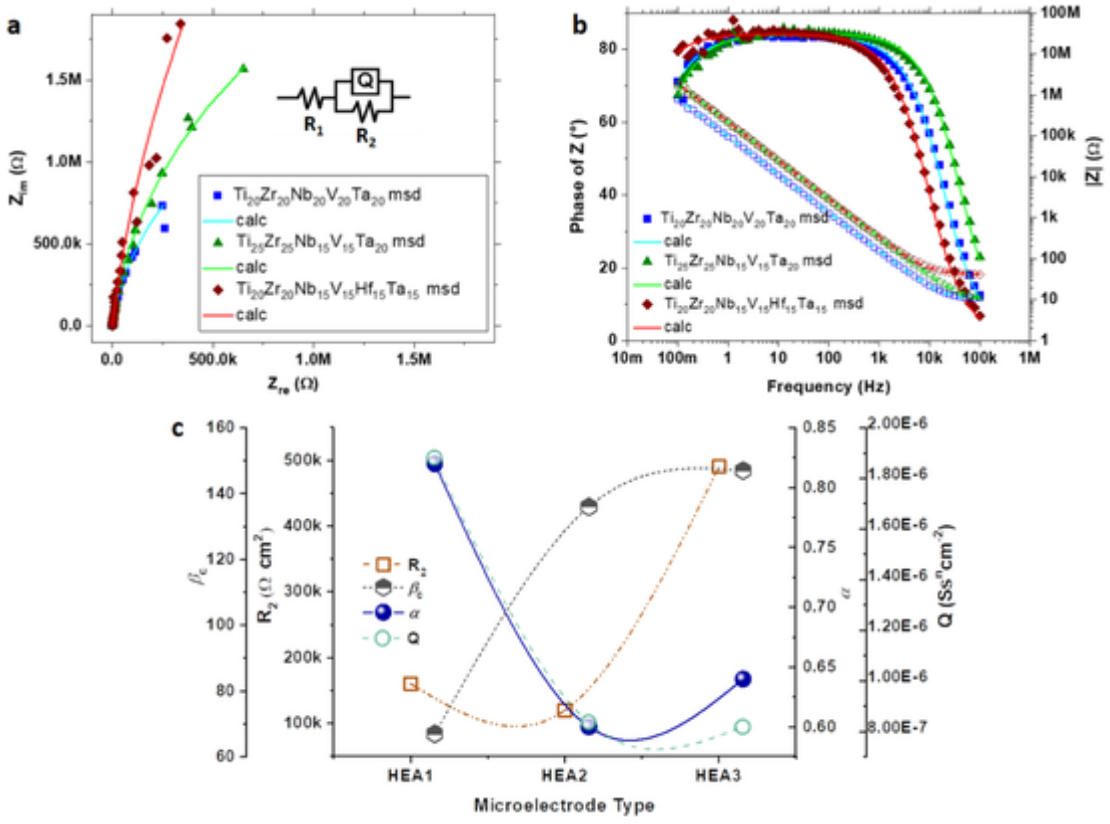

Fig. 4. (a) Nyquist plots of the HEA compositions measured at open circuit potential (scatter) and their fittings (line) with the $R(QR)$ circuit. (b) Bode phase (filled scatter) and magnitude (empty scatter) plots and the corresponding ECM fittings (Bode phase – straight line, magnitude – dashed line). (c) Comparison of the R_2 and Q_0 parameters obtained from ECM, β_c from the Tafel fitting and α from the B–V model.

Table 4
Parameters for each alloy retrieved from the equivalent circuit model. R_1 = solution resistance, R_2 = charge transfer resistance and Q_0 = double-layer capacitance parameter of the bulk electrode.

Electrode type	R_1 (Ω cm^2) ($\pm$ 0.05)	R_2 (Ω cm^2) ($\pm$ 1.9 $\times 10^3$)	Q_0 (S s^n cm^{-2}) ($\pm$ 2.3 $\times$ 10^{-8})	n (–) ($\pm$ 0.01)	Chi-squared
HEA1	0.47	1.6 $\times$ 10^5	1.9 $\times$ 10^{-6}	0.93	1.87 $\times$ 10^{-3}
HEA2	0.22	1.2 $\times$ 10^5	8.4 $\times$ 10^{-7}	0.94	1.11 $\times$ 10^{-3}
HEA3	0.98	4.9 $\times$ 10^5	8.2 $\times$ 10^{-7}	0.94	1.96 $\times$ 10^{-3}

HAADF-STEM image in Fig. S1b presents the existence of the natural oxide layer (indicated by the blue arrow). This native oxide layer on the HEA2 (single phase BCC structure confirmed by the selected area electron diffraction (SAED) in Fig. S1c) is only ~ 1.5 nm registered by the high-resolution transmission electron microscopy (HRTEM) in Fig. S1d. The native oxide is Zr and Ti-rich (25 at% Zr, 16 at% Ti, 9 at% Nb, 8 at% Ta, 8 at% V) as determined in the energy dispersive X-ray mode (EDX). After conducting the polarization test in 1 M KOH solution, Fig. 5a shows the overall HAADF image of the cross-section after polarization, whereas Fig. 5b depicts the correlated SAED pattern. HRTEM images recorded from these regions confirm the 5 nm oxide layer (Fig. 5c). HAADF image and the corresponding EDX spectra indicated the composition of this oxide layer composed of Zr (22 at%), Ti (8 at%), V (6 at%), Ta (5 at%) and Nb (4 at%) (Fig. 5d and e). Here, the Ti/Zr ratio after LSV is determined as 0.36. A similar surface layer oxide can be observed along the surface of the HEA3 electrode (Fig. S2a and b). A slightly thicker oxide layer of 6.5 nm is observed for this composition after the polarization test (Fig. S2c). In contrast to HEA2, HAADF and EDX imaging confirm the increase in TiO_x (Ti/Zr = 0.77) after LSV (Fig. S3). This finding indicates that the material with the lowest corrosion rate (HEA3) has the highest Ti content within the oxide layer. No clear difference in terms of the surface morphology is observed by SEM when the region after immersion in 1 M KOH solution for 1 h (Fig. S4a) compared to the as-sputtered microfiber region (Fig. S4b). The solidified surface during sputtering can be better visualized with optical micrography (Fig. S4c).

3.7. Polarization behavior in acidic and saline environments

In order to show the corrosion resistance of these alloys in acidic and saline environments, the representative HEA2 electrode was tested. Fig. 6 shows the response of the electrodes in 0.5 M H_2SO_4 (violet curve) and 0.9% NaCl (dark cyan curve) at room temperature. From these curves, one can determine the corrosion current densities as 13.31 and 7.29 μA cm^{-2} for the acidic and saline environments, respectively. The j_{corr} for SS 304 and AlCoCrFeNi HEA were determined as 45.3 and 13.1 μA cm^{-2} in 0.5 M H_2SO_4, respectively, indicating a superior or similar performance for the HEA2 [44]. For the Mg0.5ZnX (X = Ca, Ge) where x = 1.0, 0.5 or 0.2. j_{corr} varies between 10 and 13 μA cm^{-2} prepared with deionized water; thus, our HEAs can be an alternative material for specific biomedical applications where the Mg-based alloys are severely affected by corrosion [45]. Using Eq. (1) and Table 2, the annual corrosion rates can be estimated as 0.148 mm yr^{-1} (in acidic solution) and 0.081 mm yr^{-1} (in saline solution). From these results, it can be deduced that the adopted high and medium alloy systems are resistant to corrosion not only in alkaline but also in acidic and saline environments.

4. Conclusions

The main conclusions are:

(1) The developed microfiber HEA electrodes were analyzed for the first time in the alkaline medium in terms of corrosion resistance and hydrogen evolution performance via linear sweep voltammetry, Tafel fitting and Butler–Volmer equation. Besides, the ionic diffusion and electron transfer kinetics were assessed via electrochemical impedance spectroscopy and simulated by an equivalent circuit model.
(2) Ultra-high corrosion resistance down to 1.85 μm yr^{-1} (HEA3) was estimated due to very small j_{corr}, performing orders of magnitude better than their conventional alloy counterparts.Furthermore, extremely high potential stability is observed for these HEA alloys, where for HEA2 the shift is only 5 mV for cyclic LSV cycles with a −0.1 V shift in onset potential for an increasing number of cycles.
(3) Low cathodic Tafel slope for HEA1 (β_c = 67 mV dec^{-1}) and high cathodic activity with a transfer coefficient α = 0.82 from B–V suggest its use for HER in alkaline media.
(4) A stable capacitive response over a wide range of frequencies with a Phase angle of ~ 85° and an almost linear decrease in the Bode magnitude profile indicates the presence of the barrier passive films stemming from the hydroxide and oxyhydroxide groups, which can be differentiated by HRTEM and HAADF-EDX before and after HER. Moreover, the R_2 is on the order of 10^6–10^7 Ω, indicating that the passive films act as a semiconducting layer against corrosion. This small passivating oxide layer formation is corroborat[Edit][Proof][PDF]TEM imaging of the cross-section of the HEA samples, where the increase in the Ti/Zr ratio within the oxide layer further increases the passivation stability.
(5) For these alloys, the corrosion resistance is only 0.148 mm yr^{-1} in acidic and 0.081 mm yr^{-1} in saline environments suggesting its durability in daily-life uses such as water-conducting pipelines, marine operations, or surgical instruments/implants.
(6) Compared to platinum group elements, HEAs are composed of economical group IVB and VB transition elements with ultra-high stability in alkaline media along with hydrogen evolution, which can be considered in battery or fuel cell applications.

CRediT authorship contribution statement

Baran Sarac: Conceptualization, Data curation, Formal analysis, Funding acquisition, Investigation, Methodology, Project administration, Validation, Writing – original draft. **Vladislav Zadorozhnyy:** Data curation, Formal analysis, Funding acquisition, Investigation, Writing – original draft. **Yurii P. Ivanov:** Formal analysis, Funding acquisition, Investigation, Methodology, Writing – original draft. **Florian Spieckermann:** Data curation, Formal analysis, Investigation. **Semen Klyamkin:** Funding acquisition, Writing – review & editing. **Elena Berdonosova:** Investigation, Formal analysis, Writing – review & editing. **Mikhail Serov:** Investigation, Funding acquisition. **Sergey Kaloshkin:** Funding acquisition, Writing – review & editing. **A. Lindsay Greer:** Funding acquisition, Writing – review & editing. **A. Sezai Sarac:** Data curation, Formal analysis, Writing – original draft. **Jürgen Eckert:** Funding acquisition, Writing – review & editing.

Declaration of Competing Interest

The authors declare that they have no known competing financial interests or personal relationships that could have appeared to influence the work reported in this paper.

Data availability

The data that support the findings of this study are available from the corresponding authors upon reasonable request.

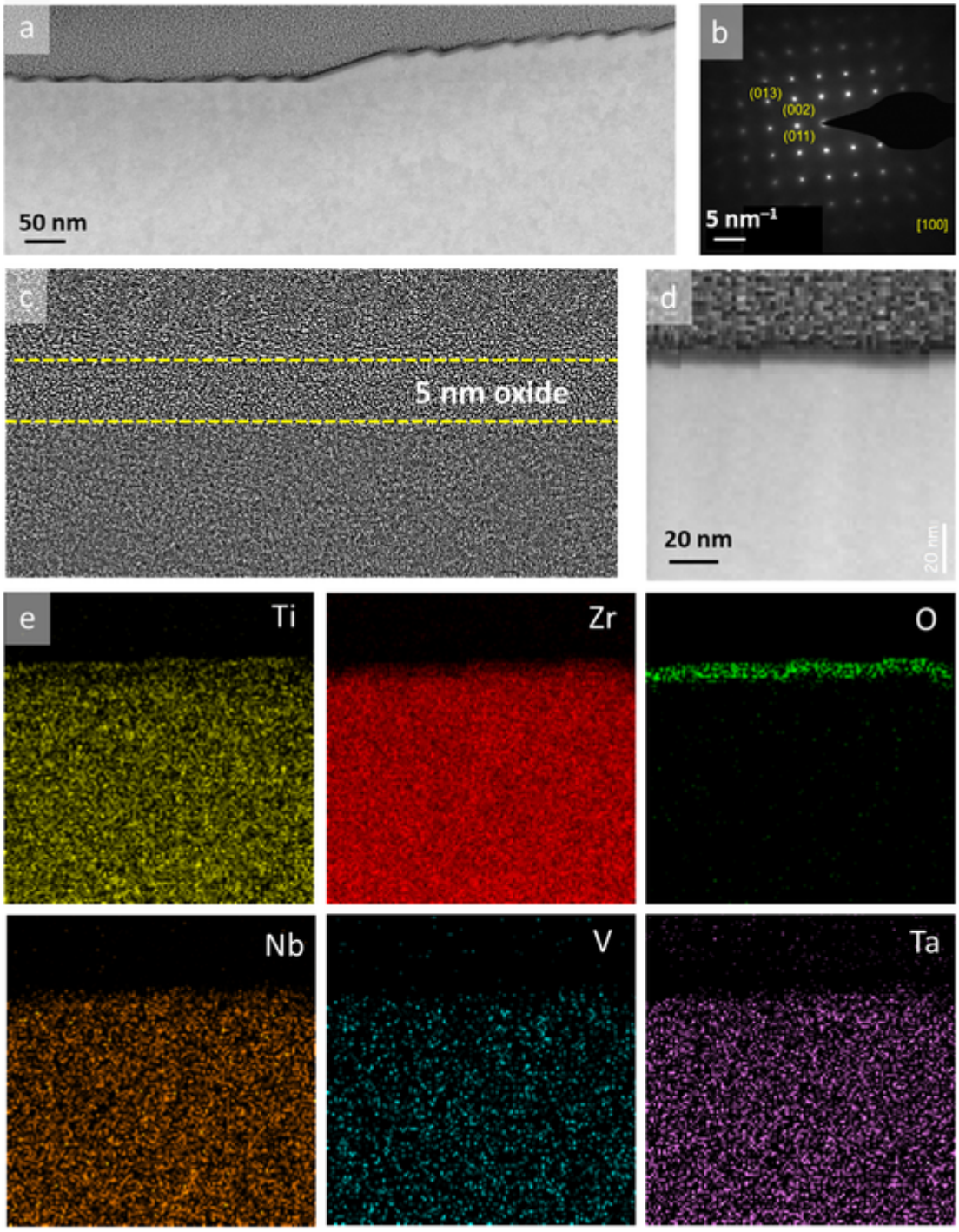

Fig. 5. (a) Overall HAADF image of the cross-section of the HEA2 after polarization in an alkaline environment. (b) SAED pattern shows the (100) pattern of the BCC structure. (c) 5 nm oxide layer is recorded, where (d) close-up HAADF imaging and (e) corresponding EDX confirm the Zr-rich oxide formation and homogeneous elemental dispersion within the HEA2.

Acknowledgments

This work was supported by The Austrian Science Fund (FWF) under project Grant I3937-N36, "ExtendGlass – Extending the range of the glassy state: Exploring structure and property limits in metallic glasses" (Grant ERC-2015-ADG-695487), the state task of the Ministry of Science and Higher Education of the Russian Federation No. 0657-2020-0005, and Ministry of Science and Higher Education of the Russian Federation in the framework of the Increase Competitiveness Program of NUST "MISiS" (Grant number K2-2020-046). We thank DESY (Hamburg, Germany), a member of the Helmholtz Association (HGF), for providing experimental facilities and the for the support of the Beamline Scientist Dr. Jochi Tseng. Parts of this research, including synchrotron X-ray diffraction, were performed at PETRA III using the Powder Diffraction and Total Scattering beamline P02.1 in the framework of project CALIPSOplus under the Grant Agreement 730872 of the EU Framework Programme for Research and Innovation HORIZON 2020.

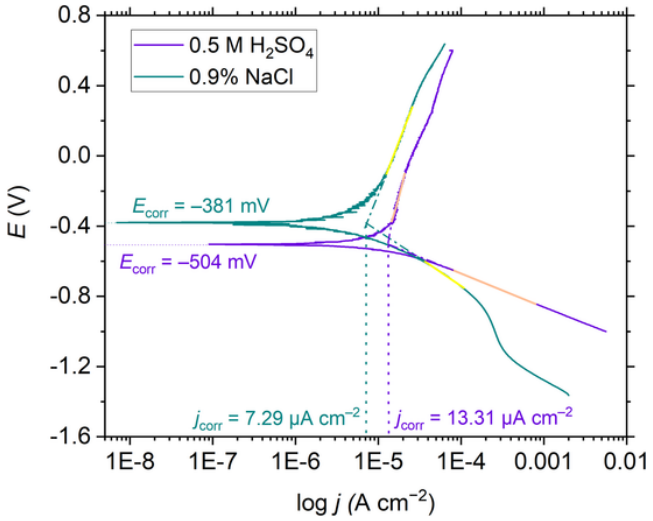

Fig. 6. Polarization behavior of HEA2 in 0.5 M H_2SO_4 (violet) and 0.9% NaCl (dark cyan) solutions. (For interpretation of the references to color in this figure legend, the reader is referred to the web version of this article.)

Appendix A. Supplementary material

Supplementary data associated with this article can be found in the online version at doi:10.1016/j.corsci.2021.109880.

References

[1] Y. Zheng, Y. Jiao, A. Vasileff, S.Z. Qiao, The hydrogen evolution reaction in alkaline solution: from theory, single crystal models, to practical electrocatalysts, Angew. Chem. Int. Ed. 57 (2018) 7568–7579.

[2] R. Subbaraman, D. Tripkovic, D. Strmcnik, K.C. Chang, M. Uchimura, A.P. Paulikas, V. Stamenkovic, N.M. Markovic, Enhancing hydrogen evolution activity in water splitting by tailoring Li^+-$Ni(OH)_2$-Pt interfaces, Science 334 (2011) 1256–1260.

[3] J.W. Yeh, S.K. Chen, S.J. Lin, J.Y. Gan, T.S. Chin, T.T. Shun, C.H. Tsau, S.Y. Chang, Nanostructured high-entropy alloys with multiple principal elements: novel alloy design concepts and outcomes, Adv. Eng. Mater. 6 (2004) 299–303.

[4] Y.F. Ye, Q. Wang, J. Lu, C.T. Liu, Y. Yang, High-entropy alloy: challenges and prospects, Mater. Today 19 (2016) 349–362.

[5] Y.J. Li, A. Savan, A. Kostka, H.S. Stein, A. Ludwig, Accelerated atomic-scale exploration of phase evolution in compositionally complex materials, Mater. Horiz. 5 (2018) 86–92.

[6] A.O. Moghaddam, E.A. Trofimov, Toward expanding the realm of high entropy materials to platinum group metals: a review, J. Alloy. Compd. 851 (2021) 156838.

[7] P.Y. Ma, M.M. Zhao, L. Zhang, H. Wang, J.F. Gu, Y.C. Sun, W. Ji, Z.Y. Fu, Self-supported high-entropy alloy electrocatalyst for highly efficient H_2 evolution in acid condition, J. Mater. 6 (2020) 736–742.

[8] G. Zhang, K. Ming, J. Kang, Q. Huang, Z. Zhang, X. Zheng, X. Bi, High entropy alloy as a highly active and stable electrocatalyst for hydrogen evolution reaction, Electrochim. Acta 279 (2018) 19–23.

[9] H.D. Li, Y. Han, H. Zhao, W.J. Qi, D. Zhang, Y.D. Yu, W.W. Cai, S.X. Li, J.P. Lai, B.L. Huang, L. Wang, Fast site-to-site electron transfer of high-entropy alloy nanocatalyst driving redox electrocatalysis, Nat. Commun. 11 (2020) 5437.

[10] B. Sarac, V. Zadorozhnyy, E. Berdonosova, Y.P. Ivanov, S. Klyamkin, S. Gumrukcu, A.S. Sarac, A. Korol, D. Semenov, M. Zadorozhnyy, A. Sharma, A.L. Greer, J. Eckert, Hydrogen storage performance of the multi-principal-component CoFeMnTiVZr alloy in electrochemical and gas–solid reactions, RSC Adv. 10 (2020) 24613–24623.

[11] V. Zadorozhnyy, B. Sarac, E. Berdonosova, T. Karazehir, A. Lassnig, C. Gammer, M. Zadorozhnyy, S. Ketov, S. Klyamkin, J. Eckert, Evaluation of hydrogen storage performance of ZrTiVNiCrFe in electrochemical and gas-solid reactions, Int. J. Hydrog. Energy 45 (2020) 5347–5355.

[12] X.W. Qiu, Corrosion behavior of $Al_2CrFeCo_xCuNiTi$ high-entropy alloy coating in alkaline solution and salt solution, Results Phys. 12 (2019) 1737–1741.

[13] Y. Xin, S.H. Li, Y.Y. Qian, W.K. Zhu, H.B. Yuan, P.Y. Jiang, R.H. Guo, L.B. Wang, High-entropy alloys as a platform for catalysis: progress, challenges, and opportunities, ACS Catal. 10 (2020) 11280–11306.

[14] T. Löffler, F. Waag, B. Gökce, A. Ludwig, S. Barcikowski, W. Schuhmann, Comparing the activity of complex solid solution electrocatalysts using inflection points of voltammetric activity curves as activity descriptors, ACS Catal. 11 (2021) 1014–1023.

[15] S. Nellaiappan, N.K. Katiyar, R. Kumar, A. Parui, K.D. Malviya, K.G. Pradeep, A.K. Singh, S. Sharma, C.S. Tiwary, K. Biswas, High-entropy alloys as catalysts for the CO_2 and CO reduction reactions: experimental realization, ACS Catal. 10 (2020) 3658–3663.

[16] M. Sahlberg, D. Karlsson, C. Zlotea, U. Jansson, Superior hydrogen storage in high entropy alloys, Sci. Rep. 6 (2016) 36770.

[17] A.R. Zeradjanin, A. Vimalanandan, G. Polymeros, A.A. Topalov, K.J.J. Mayrhofer, M. Rohwerder, Balanced work function as a driver for facile hydrogen evolution reaction – comprehension and experimental assessment of interfacial catalytic descriptor, Phys. Chem. Chem. Phys. 19 (2017) 17019–17027.

[18] J.L. Lv, H.J. Jin, Corrosion resistance mechanism of the passive films formed on as-cast FeCoCrNiMn high-entropy alloy, Mater. Res. Express 7 (2020) 016592.

[19] A. Raza, S. Abdulahad, B. Kang, H.J. Ryu, S.H. Hong, Corrosion resistance of weight reduced $Al_xCrFeMoV$ high entropy alloys, Appl. Surf. Sci. 485 (2019) 368–374.

[20] S.P. Wang, J. Xu, TiZrNbTaMo high-entropy alloy designed for orthopedic implants: as-cast microstructure and mechanical properties, Mater. Sci. Eng. C 73 (2017) 80–89.

[21] E. Fazakas, B. Varga, V. Geanta, T. Berecz, P. Jenei, I. Voiculescu, M. Cosnita, R. Stefanoiu, Microstructure, thermal, and corrosion behavior of the AlAgCuNiSnTi equiatomic multicomponent alloy, Materials 12 (2019) 926.

[22] Q.T. Song, J. Xu, $(TiZrNbTa)_{90}Mo_{10}$ high-entropy alloy: electrochemical behavior and passive film characterization under exposure to Ringer's solution, Corros. Sci. 167 (2020) 108513.

[23] B. Sarac, T. Karazehir, M. Mühlbacher, A.S. Sarac, J. Eckert, Electrocatalytic behavior of hydrogenated Pd-metallic glass nanofilms: Butler-Volmer, Tafel, and impedance analyses, Electrocatalysis 11 (2020) 94–109.

[24] K.S. Senkevich, M.M. Serov, O.Z. Umarova, Fabrication of intermetallic titanium alloy based on Ti2AlNb by rapid quenching of melt, Met. Sci. Heat Treat. 59 (2017) 463–466.

[25] O.K. Fatkulin, G.B. Stroganov, A.A. Il'in, The Metal Science and Technology of Rapidly Quenched Alloys, MAI, Moscow, 2009 (in Russian).

[26] V.N. Antsiferov, M.M. Serov, V.P. Lezhnin, A.A. Smetkin, On production, properties, and application of quick-cooled fibers, Izv. Vysh. Uchebn. Zaved. Poroshk. Metall. Funkts. Pokryt. 1 (2013) 55–58.

[27] V.N. Antsiferov, M.M. Serov, V.P. Lezhnin, A.A. Smetkin, About fabrication, properties and application of rapidly cooled fibers, Izv. Vysh. Uchebn. Zaved. Poroshk. Metall. Funkts. Pokryt. 4 (2011) 36–40.

[28] M.M. Serov, Microcrystalline and amorphous alloys obtained by the method of rapid quenching of melt, Tekhnol. Legk. Splav. 4 (2008) 40–43.

[29] P. Konik, E. Berdonosova, I. Savvotin, V. Zadorozhnyy, M. Zadorozhnyy, D. Semenov, A. Korol, A. Kvaratskheliya, S. Klyamkin, Structure and hydrogenation features of mechanically activated $LaNi_5$-type alloys, Int. J. Hydrog. Energy 46 (2020) 13638–13646.

[30] W. Wang, X. Wei, D. Choi, X. Lu, G. Yang, C. Sun, Chapter 1 – electrochemical cells for medium- and large-scale energy storage: fundamentals, in: C. Menictas, M. Skyllas-Kazacos, T.M. Lim (Eds.), Advances in Batteries for Medium and Large-Scale Energy Storage, Woodhead Publishing, 2015, pp. 3–28.

[31] J.Y. Wang, W.H. Li, H.L. Yang, H. Huang, S.X. Ji, J.M. Ruan, Z.L. Liu, Corrosion behavior of CoCrNi medium-entropy alloy compared with 304 stainless steel in H_2SO_4 and NaOH solutions, Corros. Sci. 177 (2020) 108973.

[32] Linear Polarization Resistance and Corrosion Rate – Theory and Background, Pine Research Instrumentation, 2016, pp. 1–14.

[33] A.J. Bard, L.R. Faulkner, Chapter 3. Kinetics of electrode reactions, Electrochemical Methods: Fundamentals and Applications, John Wiley & Sons, Inc., United States of America, 01/2001, pp. 98–102.

[34] S. Anantharaj, S. Noda, V.R. Jothi, S. Yi, M. Driess, P.W. Menezes, Strategies and perspectives to catch the missing pieces in energy-efficient hydrogen evolution reaction in alkaline media, Angew. Chem. Int. Ed. 60 (2021) 18981–19006.

[35] Y. Zhang, J. Xiao, Q.Y. Lv, S. Wang, Self-supported transition metal phosphide based electrodes as high-efficient water splitting cathodes, Front. Chem. Sci. Eng. 12 (2018) 494–508.

[36] J. Durst, A. Siebel, C. Simon, F. Hasche, J. Herranz, H.A. Gasteiger, New insights into the electrochemical hydrogen oxidation and evolution reaction mechanism, Energy Environ. Sci. 7 (2014) 2255–2260.

[37] K. Krischer, E.R. Savinova, in: G. Ertl, H. Knözinger, F. Schüth, J. Weitkamp (Eds.), Handbook of Heterogeneous Catalysis, Wiley-VCH, Chichester, 2009, pp. 1873–1905.

[38] K.J.P. Schouten, M.J.T.C. van der Niet, M.T.M. Koper, Impedance spectroscopy of H and OH adsorption on stepped single-crystal platinum electrodes in alkaline and acidic media, Phys. Chem. Chem. Phys. 12 (2010) 15217–15224.

[39] The Butler–Volmer Model, SNU Open Courseware.

[40] H.V.M. Hamelers, A. ter Heijne, N. Stein, R.A. Rozendal, C.J.N. Buisman, Butler-Volmer-Monod model for describing bio-anode polarization curves, Bioresour. Technol. 102 (2011) 381–387.

[41] Y.M. Wang, D.D. Zhao, Y.Q. Zhao, C.L. Xu, H.L. Li, Effect of electrodeposition temperature on the electrochemical performance of a $Ni(OH)_2$ electrode, RSC Adv. 2 (2012) 1074–1082.

[42] B. Sarac, V. Zadorozhnyy, Y.P. Ivanov, A. Kvaratskheliya, S. Ketov, T. Karazehir, S. Gumrukcu, E. Berdonosova, M. Zadorozhnyy, M. Micusik, M. Omastova, A.S. Sarac, A.L. Greer, J. Eckert, Surface-governed electrochemical hydrogenation in FeNi-based metallic glass, J. Power Sources 475 (2020) 228700.

[43] B. Sarac, Y.P. Ivanov, T. Karazehir, M. Mühlbacher, B. Kaynak, A.L. Greer, A.S. Sarac, J. Eckert, Ultrahigh hydrogen-sorbing palladium metallic-glass nanostructures, Mater. Horiz. 6 (2019) 1481–1487.

[44] Y.F. Kao, T.D. Lee, S.K. Chen, Y.S. Chang, Electrochemical passive properties of $Al_xCoCrFeNi$ (x = 0, 0.25, 0.50, 1.00) alloys in sulfuric acids, Corros. Sci. 52 (2010) 1026–1034.

[45] P.L. Jiang, C. Blawert, N. Scharnagl, M.L. Zheludkevich, Influence of water purity on the corrosion behavior of Mg0.5ZnX (X = Ca, Ge) alloys, Corros. Sci. 153 (2019) 62–73.